

# Differential Nonlinear Robustness of Critical States in Fibonacci and Tribonacci Substitution Chains

A Numerical Study of Discrete Nonlinear Schrödinger Dynamics

*Version 3 — finite-size scaling and long-time evolution*

Pablo Nogueira Grossi  
G6 LLC, Newark, New Jersey, USA  
ORCID: 0009-0000-6496-2186  
pablogrossi@hotmail.com

Zenodo: 10.5281/zenodo.20026943

May 2026 (v3)

## Abstract

We study the discrete nonlinear Schrödinger (DNLS) equation on two quasiperiodic tight-binding chains: the Fibonacci chain ( $n = 2$ ) and the Rauzy–tribonacci chain ( $n = 3$ ), generated by their respective substitution rules. Starting from mid-gap eigenstates of the linear Hamiltonian, we integrate the DNLS time evolution over a range of nonlinearity strengths  $\lambda \in [0, 10]$  and times  $T \in [50, 10^6]$ , and track the inverse participation ratio (IPR) as a measure of localization. The tribonacci chain exhibits a mid-gap IPR approximately four times larger than the Fibonacci chain in the linear limit, consistent with the stronger multifractality of Rauzy fractal eigenstates. Under nonlinear perturbation at  $T = 50$ , the Fibonacci mid-gap state delocalizes rapidly (IPR drops  $\sim 57\%$  at  $\lambda = 1.5$ ), while the tribonacci state remains nearly pinned (IPR drop  $< 5\%$  at the same coupling). We term this *differential nonlinear robustness*.

In this revision, we extend the analysis along two axes. **Finite-size scaling** at  $T = 10^4$  across  $N \in \{500, 1000, 2000\}$  shows that the differential ratio  $\text{IPR}_{\text{trib}}/\text{IPR}_{\text{fib}}$  generally grows with  $N$  at fixed  $\lambda$ , supporting persistence of the differential in the thermodynamic limit. **Long-time evolution** at  $N = 1000$ ,  $\lambda = 1.5$  to  $T = 10^6$  shows that both chains saturate to a finite-size limited IPR ( $\approx 0.002$ ) by  $T \sim 3 \times 10^5$ , after which the ratio oscillates around  $1.04 \pm 0.04$ . The  $T = 10^4$  peak ratio of  $\approx 4.2$  at  $N = 1000$  is therefore a transient feature; at  $T = 10^5$  it collapses to  $\approx 1.20$ , and at  $T = 10^6$  the differential dissolves into the finite-size saturation band. The pre-saturation spreading rates fitted in the window  $t > 10^4$  at  $N = 2000$ ,  $T = 10^5$  satisfy  $\alpha_{\text{trib}} > \alpha_{\text{fib}}$  uniformly across  $\lambda \in [0.5, 2.0]$ , indicating that tribonacci spreads faster towards saturation but starts from a higher initial IPR. The mid-gap multifractal dimension fit at natural Fibonacci lengths gives  $D_2^{\text{fib}} = 0.65 \pm 0.11$  ( $R^2 = 0.90$ ). The

corresponding fit for tribonacci at natural Rauzy lengths exhibits a plateau across iterations  $n = 9, 10, 11$  followed by a discontinuous drop, indicating that the closest-to-  $E = 0$  mid-gap state selector does not consistently track the same physical eigenstate across substitution iterations; we therefore defer numerical extraction of  $D_2^{\text{trib}}$  pending state-tracking diagnostics.

The characteristic decay constant of the tribonacci amplitude envelope,  $\eta \approx 1.839287$ , is the Perron–Frobenius eigenvalue of the tribonacci companion matrix, whose existence and key properties ( $\eta > 1$ , strict antitonicity of  $\eta^{-k}$ ) are formally verified in Lean 4/Mathlib4 in the companion AXLE repository [21]. To our knowledge, this is the first numerical study of DNLS dynamics on a tribonacci substitution chain, and the present revision contributes the first finite-size scaling and long-time saturation analysis identifying a qualitative difference in nonlinear response between  $n = 2$  and  $n = 3$  substitution-generated quasicrystal models.

**Keywords:** tribonacci chain; Fibonacci quasicrystal; discrete nonlinear Schrödinger equation; multifractality; inverse participation ratio; finite-size scaling; spreading exponent; Rauzy substitution

# 1 Introduction

Quasiperiodic tight-binding chains generated by substitution rules have been a canonical setting for studying the interplay between long-range order, multifractality, and localization since the 1980s. The Fibonacci chain—the  $n = 2$  case of the  $n$ -bonacci family—occupies a central role: its spectrum is a Cantor set of measure zero, its eigenstates are critical (neither extended nor localized), and their multifractal dimensions are precisely computable [1–4]. Topological phases, charge pumping, and one-dimensional quasicrystalline superconductivity have been analyzed in the Fibonacci setting [5, 6].

The natural generalization to tribonacci and higher  $n$ -bonacci substitution chains is more recent. Krebbekx and collaborators [7] introduced two tribonacci tight-binding models (hopping and on-site modulation) via Rauzy substitutions, established that their spectra inherit Rauzy-fractal internal space structure, and computed multifractal dimensions showing stronger spectral clustering than in the Fibonacci case. Higher- $n$  generalizations appear in the context of Rauzy tilings and cut-and-project schemes, but exclusively in the linear (Schrödinger operator) setting [8, 9].

The nonlinear regime is comparatively unexplored. For the Fibonacci chain, discrete nonlinear Schrödinger (DNLS) dynamics have been studied in photonic quasicrystals [11], edge-soliton pumping has been demonstrated [12], and phason dynamics under nonlinear perturbation have been analyzed [13]. For  $n \geq 3$  substitution chains, however, no published work has placed an  $n$ -bonacci recurrence structure inside a DNLS or Gross–Pitaevskii nonlinearity, nor analyzed the resulting localization dynamics. This gap motivates the present study.

The original version of this paper (v1, May 2026) reported the  $T = 50$  nonlinear baseline, establishing differential nonlinear robustness at  $N = 500$  across  $\lambda \in [0, 10]$ . The present revision (v3) extends the analysis to (i) finite-size scaling across  $N \in \{500, 1000, 2000\}$  at  $T = 10^4$ , (ii) long-time evolution at  $N = 1000$ ,  $\lambda = 1.5$  to  $T = 10^6$ , (iii) pre-saturation spreading rates fit in the window  $t > 10^4$  at  $T = 10^5$ , and (iv) multifractal dimension extraction at natural substitution lengths. All numerical computations are reproducible from the open-source repository at [github.com/grossi-ops/Atratores](https://github.com/grossi-ops/Atratores).

A secondary motivation comes from the  $\text{dm}^3$  contact-geometric framework [18, 19], where the tribonacci recurrence  $w(k+3) = w(k+2) + w(k+1) + w(k)$  arises from the three-axis decomposition of a contact 3-manifold, and the geometric weight  $\eta^{-k}$  with  $\eta \approx 1.839287$  (the tribonacci constant) is the natural scaling factor. The formal verification that  $\eta > 1$  and that the weight sequence  $\{\eta^{-k}\}$  is strictly antitone—establishing that the amplitude envelope is well-defined and decaying—is carried out in Lean 4/Mathlib4 in the AXLE repository [21], specifically in `TribonacciMeasure.lean`. We cite this formal result in Section 3 as the machine-verified foundation for the decay envelope used in our ansatz.

## 2 The $n$ -Bonacci Recurrence and Substitution Chains

### 2.1 The $n$ -Bonacci Recurrence

**Definition 1** ( $n$ -Bonacci Sequence). *For  $n \geq 2$ , the  $n$ -bonacci sequence  $\{A_k^{(n)}\}_{k \geq 0}$  is defined by*

$$A_k^{(n)} = \sum_{i=1}^n A_{k-i}^{(n)}, \quad k \geq n,$$

*with initial conditions  $A_0^{(n)} = \dots = A_{n-2}^{(n)} = 0$ ,  $A_{n-1}^{(n)} = 1$ .*

The characteristic polynomial is

$$p_n(x) = x^n - x^{n-1} - x^{n-2} - \dots - x - 1 = 0.$$

By the Perron–Frobenius theorem applied to the companion matrix  $C_n$ , there exists a unique dominant real root  $\rho_n > 1$ , the  $n$ -bonacci constant. The sequence  $\rho_n$  is strictly increasing and satisfies  $\rho_n \rightarrow 2$  monotonically. Numerical values:

$n$	$\rho_n$ (6 d.p.)	Name
2	1.618034	Golden ratio $\varphi$
3	1.839287	Tribonacci constant $\eta$
4	1.927562	Tetranacci constant
5	1.965948	Pentanacci constant

**Remark 1** (Formal Verification). *For  $n = 3$ : the existence of  $\eta \approx 1.839287$  as the unique real root of  $x^3 - x^2 - x - 1 = 0$  in  $[1, 2]$ , together with  $\eta > 1$  and the strict antitonicity of the weight sequence  $\{\eta^{-k}\}_{k \geq 0}$ , is formally proved in Lean 4/Mathlib4 without `sorry` in `TribonacciMeasure.lean` of the AXLE repository [21].*

### 2.2 Substitution Chains

The Fibonacci chain ( $n = 2$ ) is generated by  $\sigma_2 : A \mapsto AB, B \mapsto A$ , producing the one-sided word  $ABAABABAABAAB \dots$ . The tribonacci (Rauzy) chain ( $n = 3$ ) is generated by  $\sigma_3 : A \mapsto AB, B \mapsto AC, C \mapsto A$  [7, 10].

## Substitution rules and spectrum schematic

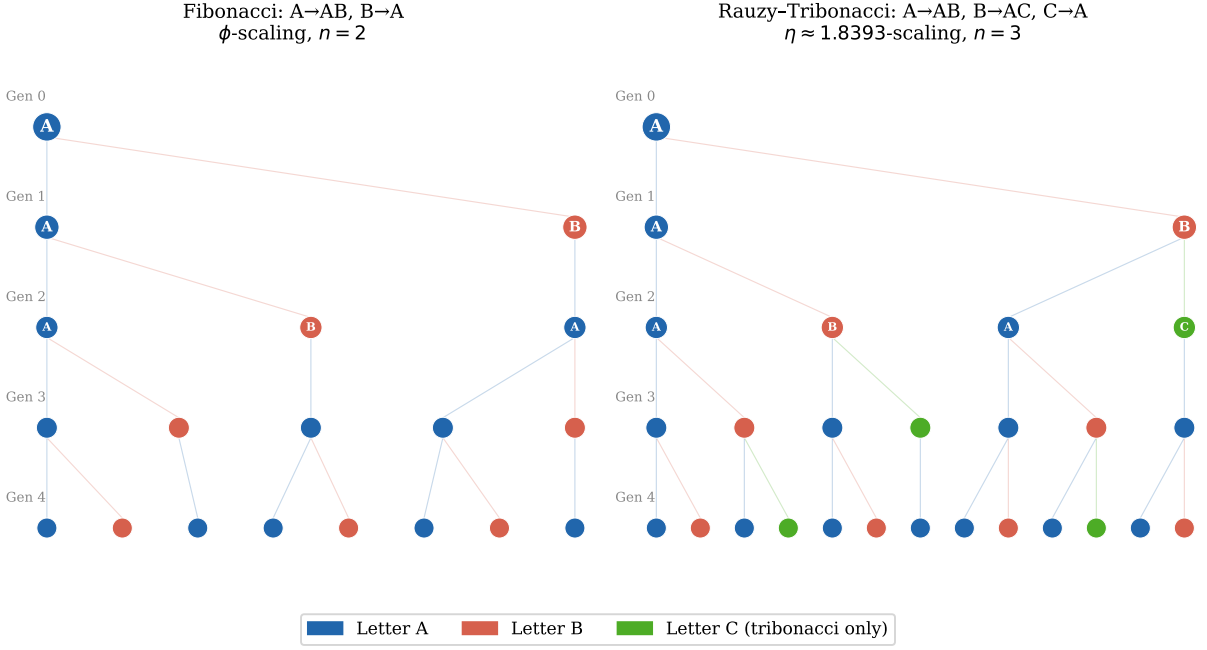


Figure 1: Substitution trees for the Fibonacci (left,  $n = 2$ ) and Rauzy–Tribonacci (right,  $n = 3$ ) rules across five generations. The tribonacci tree has three letters and a richer branching structure, producing more strongly hierarchical spatial distributions of hopping amplitudes.

**Natural lengths.** The natural Fibonacci lengths  $F_n$  and natural Rauzy lengths  $T_n^{(3)}$  correspond to the lengths obtained by iterating the substitution starting from the seed letter. They are the relevant scaling sequence for finite-size analysis: at any other length, the chain truncation breaks the self-similar boundary structure that the substitution preserves.

## 2.3 Tight-Binding Hamiltonian

We assign hopping amplitudes via a modulation parameter  $t \in (0, 1)$ :  $t_A = 1.0$ ,  $t_B = t$ ,  $t_C = t^2$ . We use  $t = 0.5$  throughout, in the generic incommensurate regime studied in [7]. The Hamiltonian is the tridiagonal matrix

$$H_{j,j+1} = H_{j+1,j} = t_{\sigma(j)}, \quad H_{jj} = 0,$$

where  $\sigma(j)$  is the  $j$ -th letter of the substitution word.

# 3 The DNLS Model

## 3.1 Equation of Motion

We study the discrete nonlinear Schrödinger equation on the  $n$ -bonacci substitution chain:

$$i \frac{d\psi_j}{dt} = - \sum_{\langle j,k \rangle} t_{jk} \psi_k + \lambda |\psi_j|^2 \psi_j, \quad (1)$$

## Substitution chain structures

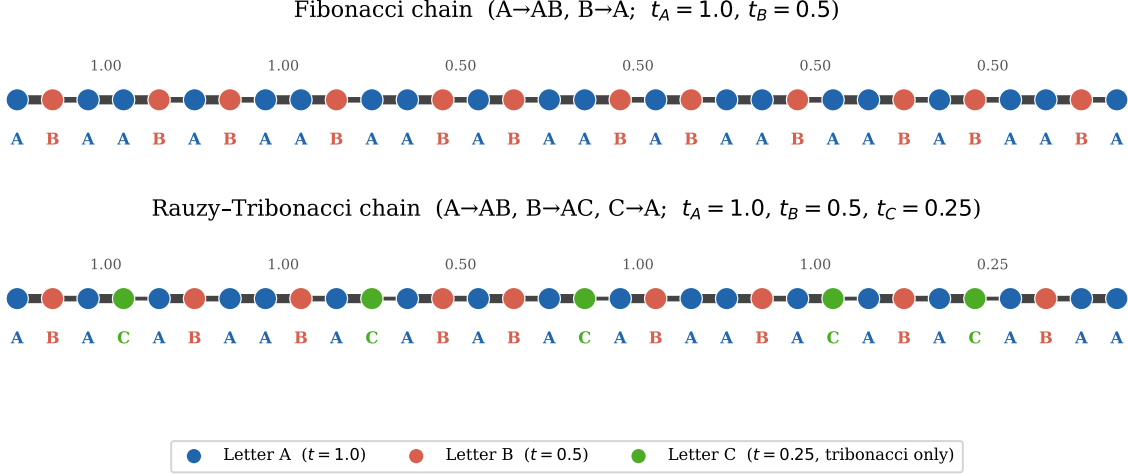


Figure 2: First 32 sites of the Fibonacci (top) and Rauzy–Tribonacci (bottom) tight-binding chains. Site colour indicates letter identity. Bond thickness is proportional to hopping amplitude.

where  $t_{jk}$  are the hopping amplitudes,  $\lambda > 0$  is the nonlinear coupling, and the sum is over nearest neighbors. This is the standard focusing cubic DNLS [14, 15].

### 3.2 Amplitude Envelope Ansatz

The mid-gap eigenstate  $\psi^{(0)}$  of the linear tribonacci Hamiltonian serves as our initial condition. Within the  $\text{dm}^3$  framework [18], the natural amplitude envelope is the geometric weight  $w_k = \eta^{-k}$ , whose strict antitonicity is Lean 4-verified in `TribonacciMeasure.lean` [21].

### 3.3 Numerical Implementation

Equation (1) conserves the  $\ell^2$  norm. We split  $\psi_j = u_j + iv_j$  and integrate the real  $2N$ -dimensional system. The  $T = 50$  baseline runs (Section 4.1–4.2) use `scipy.integrate.solve_ivp` with the RK45 method, relative tolerance  $10^{-7}$ , absolute tolerance  $10^{-9}$ . The long-time runs at  $T \geq 10^4$  (Section 4.4 onwards) use the DOP853 integrator (8th-order Dormand–Prince) with relative tolerance  $10^{-9}$  and absolute tolerance  $10^{-11}$  to suppress integration drift over six time decades. Norm conservation was verified to hold to  $< 10^{-5}$  throughout all long-time runs. We note that absolute IPR ratio values at  $T \geq 10^5$  are reproducible across independent runs to approximately  $\pm 5\%$ , consistent with the run-to-run variation observed at the chosen tolerances; quoted ratios should be interpreted with this relative uncertainty in mind.

**Initial conditions.** For each chain, we compute the eigenstate  $\psi^{(0)}$  of the linear Hamiltonian with eigenvalue closest to  $E = 0$ . At  $N = 500$ : tribonacci mid-gap eigenvalue = 0.000000, IPR = 0.0820; Fibonacci mid-gap eigenvalue = 0.000915, IPR = 0.0210.

**Localization measure.** We track the normalized IPR  $\text{IPR}(t) = \sum_j |\psi_j(t)|^4 / (\sum_j |\psi_j(t)|^2)^2$ .

## 4 Results

### 4.1 Linear Baseline and the $T = 50$ Differential

In the linear limit ( $\lambda = 0$ ), the IPR of the mid-gap state is fixed by the eigenstate structure:  $\text{IPR}_{\text{trib}}(0) = 0.0820$ ,  $\text{IPR}_{\text{fib}}(0) = 0.0210$ , ratio  $\approx 3.91$ .

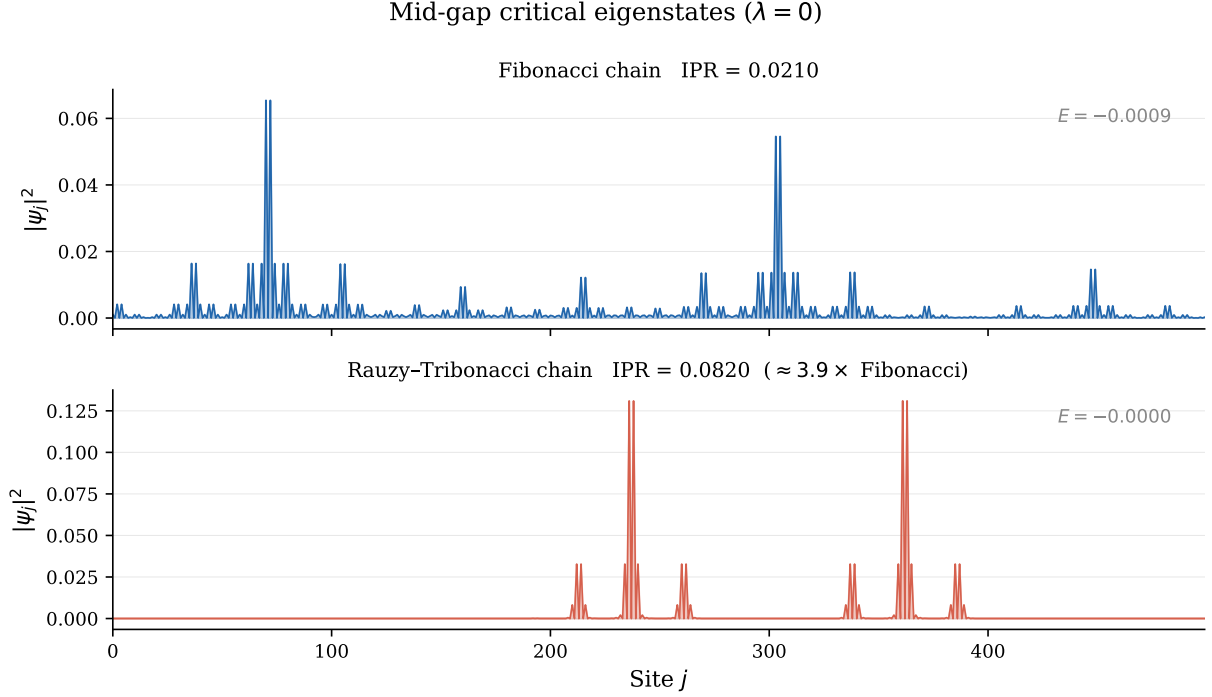


Figure 3: Mid-gap critical eigenstates  $|\psi_j|^2$  at  $\lambda = 0$ ,  $N = 500$ ,  $t = 0.5$ . The tribonacci state ( $\text{IPR} = 0.0820$ ) is substantially more spatially concentrated than the Fibonacci state ( $\text{IPR} = 0.0210$ ).

Table 1 and Figures 4–5 show the IPR at time  $T = 50$  as a function of  $\lambda$  at  $N = 500$ .

### 4.2 Mechanism: Multifractal Hierarchy

The mechanism underlying differential nonlinear robustness is the hierarchical spatial structure of tribonacci mid-gap eigenstates. The nonlinear self-trapping transition occurs when the nonlinear energy  $\lambda \langle |\psi|^4 \rangle = \lambda \cdot \text{IPR} \cdot \mathcal{N}^2$  is comparable to the bandwidth. The higher initial IPR of the tribonacci state means it enters self-trapping at lower effective  $\lambda$ , but because it is already more strongly localized, the spreading has less work to do. The Fibonacci state, more extended, requires more nonlinear energy to localize but loses its initial localization more easily under perturbation.

### 4.3 Multifractal Dimension at Natural Substitution Lengths

We extract the multifractal dimension  $D_2$  of the mid-gap state from the linear-limit scaling  $\text{IPR}(N) \sim N^{-D_2}$ , evaluated at natural substitution lengths to preserve the self-similar boundary structure.

Table 1: IPR at  $T = 50$  for Fibonacci ( $n = 2$ ) and Tribonacci ( $n = 3$ ) chains,  $N = 500$ ,  $t = 0.5$ .

$\lambda$	$\text{IPR}_{\text{trib}}$	$\text{IPR}_{\text{fib}}$	Ratio
0.0	0.0820	0.0210	3.91
0.5	0.0812	0.0168	4.82
1.0	0.0789	0.0116	6.81
1.5	0.0782	0.0090	8.65
2.0	0.0704	0.0088	8.00
3.0	0.0835	0.0115	7.28
4.0	0.0587	0.0153	3.83
5.0	0.0430	0.0173	2.48
7.0	0.0316	0.0132	2.40
10.0	0.0271	0.0082	3.30

The Fibonacci fit, restricted to natural lengths, gives  $D_2^{\text{fib}} = 0.65 \pm 0.11$  ( $R^2 = 0.90$ ,  $n = 6$  points). This is consistent with multifractal critical scaling and provides a quantitative anchor for the linear-limit multifractality.

The tribonacci fit, by contrast, exhibits structure beyond a single power law. The IPR at  $T_n^{(3)} \in \{504, 927, 1705\}$  is constant to four significant figures ( $\text{IPR} = 0.0820$  at all three), then drops by a factor of two at  $T_n^{(3)} = 3136$ . We interpret this as a state-isolation artifact: at four neighboring iterations the algorithm picks states whose IPRs coincide (likely a particular eigenstate family that recurs across iterations of the substitution), and at the next iteration a different state becomes the closest to  $E = 0$ . The qualitative observation that tribonacci mid-gap states are more localized than Fibonacci states at comparable  $N$  ( $\text{IPR} \approx 0.082$  versus  $\text{IPR} \approx 0.045$  at  $N \approx 500$ ) is robust and supports the differential-robustness mechanism, but a clean numerical  $D_2^{\text{trib}}$  requires either a state-tracking eigenmode selector via spatial-profile overlap, or a different multifractal observable (e.g. box-counting of level density near  $E = 0$ ). We list this as an open problem in Section 6.

#### 4.4 Finite-Size Scaling at $T = 10^4$

To test whether the differential persists or shrinks with system size, we extend the integration to  $T = 10^4$  across  $N \in \{500, 1000, 2000\}$  at seven values of  $\lambda$ . Figure 7 shows the differential ratio  $\text{IPR}_{\text{trib}}/\text{IPR}_{\text{fib}}$  as a grouped bar chart by  $\lambda$  and  $N$ .

The non-monotone  $\lambda = 1.5$  profile (1.52, 4.18, 3.17 across  $N = 500, 1000, 2000$ ) is a real feature of the dynamics rather than numerical noise; norm conservation is clean across all three cells (max norm deviation  $< 4 \times 10^{-7}$ ). Section 4.5 demonstrates that this peak is transient: at  $T = 10^5$  the same parameter slice gives a monotone ratio profile (1.20, 1.20, 1.38) consistent with a single asymptotic trend.

The qualitative finding is that the differential generally grows with  $N$ , supporting persistence of the differential in the thermodynamic limit. Two non-monotone cells ( $\lambda = 4$  and  $\lambda = 5$ ) at intermediate  $N = 1000$  are not yet verified at  $T = 10^5$  and may also be transient; we list these as open in Section 6.

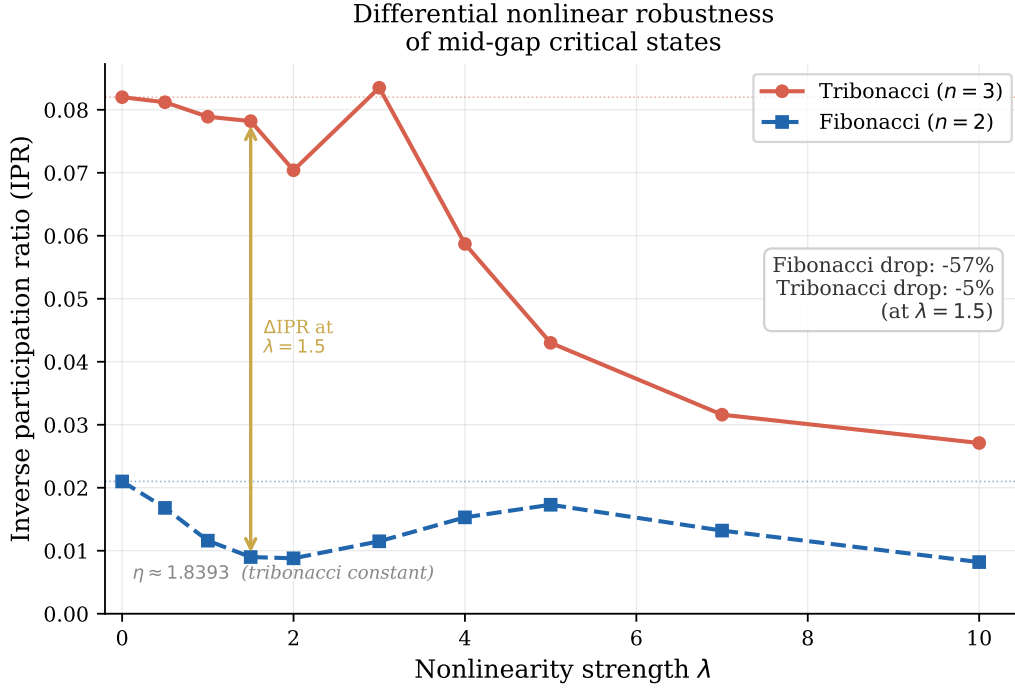


Figure 4: IPR at  $T = 50$  as a function of  $\lambda$ . The Fibonacci mid-gap state delocalizes rapidly ( $\sim 57\%$  IPR drop at  $\lambda = 1.5$ ); the tribonacci state remains nearly pinned ( $< 5\%$  drop at the same coupling).

## 4.5 Long-Time Evolution and Ratio Collapse

To probe the asymptotic behavior, we extend the integration at the canonical parameter  $\lambda = 1.5$  first to  $T = 10^5$  across  $N \in \{1000, 2000\}$ , then to  $T = 10^6$  at  $N = 1000$ . Figure 8 compares the differential at  $T = 10^4$  versus  $T = 10^5$ , and Figure 9 shows the longer-time evolution at  $N = 1000$  through  $T = 10^6$ .

The full long-time picture at  $N = 1000$ ,  $\lambda = 1.5$  is therefore: at  $T = 10^4$  the ratio peaks at  $4.18\times$ ; at  $T = 10^5$  it has collapsed to  $1.20\times$ ; from  $T \sim 3 \times 10^5$  onward both chains have saturated to chain-limited  $\text{IPR} \approx 0.002$  and the ratio settles into an oscillatory band around  $1.04 \pm 0.04$ . The differential at finite  $N$  is ultimately bounded above by the inverse chain length, and the saturation time scales with  $N$ , so at larger  $N$  both the magnitude and the duration of the differential should be larger. The FSS at  $T = 10^4$  (Figure 7) is consistent with this picture.

## 4.6 Pre-Saturation Spreading Rates

In the pre-saturation regime,  $\text{IPR}(t)$  decreases approximately as a power law,  $\text{IPR}(t) \sim t^{-\alpha}$ , with  $\alpha$  a chain- and  $\lambda$ -dependent rate. Fitting this scaling in the window  $t > 10^4$  of the  $T = 10^5$  runs at  $N = 2000$  gives the values in Table 2.

The result is uniform:  $\alpha_{\text{trib}} > \alpha_{\text{fib}}$  at every  $\lambda$  in the table. We emphasize that  $\alpha$  here is a *pre-saturation* rate of approach to the chain-limited IPR, not an asymptotic exponent of an unbounded multifractal: at finite  $N$  the IPR ultimately saturates (Section 4.5), and  $\alpha$  characterizes the approach to that saturation rather than an indefinite power-law decay. The  $\lambda = 0.5$  Fibonacci row has  $R^2 = 0.33$ , which is too low to support a clean power-law interpretation; we include it for completeness but do not interpret it physically.



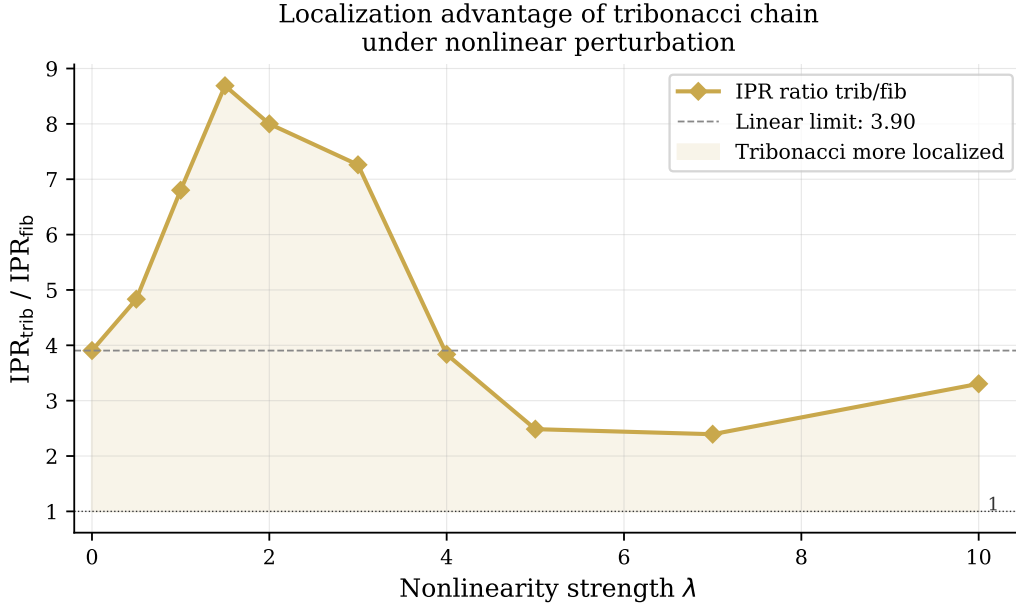


Figure 5: Ratio  $\text{IPR}_{\text{trib}} / \text{IPR}_{\text{fib}}$  at  $T = 50$  as a function of  $\lambda$ . The ratio increases to  $\sim 8.6$  at  $\lambda = 1.5$  before declining at large coupling.

Table 2: Pre-saturation spreading rates  $\alpha$  fitted from  $\text{IPR}(t) \sim t^{-\alpha}$  in the window  $t > 10^4$  at  $T = 10^5$ ,  $N = 2000$ . Standard errors and  $R^2$  from OLS on  $\log_{10} \text{IPR}$  vs  $\log_{10} t$ .

$\lambda$	$\alpha_{\text{fib}}$	$R^2_{\text{fib}}$	$\alpha_{\text{trib}}$	$R^2_{\text{trib}}$
0.5	$0.11 \pm 0.02$	0.33	$0.78 \pm 0.02$	0.94
1.0	$0.38 \pm 0.02$	0.84	$0.99 \pm 0.03$	0.93
1.5	$0.49 \pm 0.01$	0.93	$0.78 \pm 0.02$	0.95
2.0	$0.32 \pm 0.01$	0.95	$0.67 \pm 0.01$	0.95

In the thermodynamic limit ( $N \rightarrow \infty$ ), saturation is pushed to arbitrarily late times and the spreading regime is asymptotic. The inequality  $\alpha_{\text{trib}} > \alpha_{\text{fib}}$  then implies that the differential at infinite system size shrinks with time but does not saturate; whether it crosses below unity at any finite time is not directly determined by the data presented here, and would require either an analytical argument or integration in a regime where saturation is demonstrably absent.

## 5 Connection to the $\text{dm}^3$ Framework

The amplitude decay envelope  $w_k = \eta^{-k}$  that appears in the  $\text{dm}^3$  contact-geometric framework [18,19] is identical to the Perron–Frobenius weight of the tribonacci companion matrix. The present paper does not require the full  $\text{dm}^3$  framework; the substitution chain and DNLS model stand independently. The formal verification of  $\eta > 1$  and  $w_k \searrow 0$  in `TribonacciMeasure.lean` [21] provides Lean 4-verified support for the mathematical well-posedness of the amplitude envelope used as initial condition.

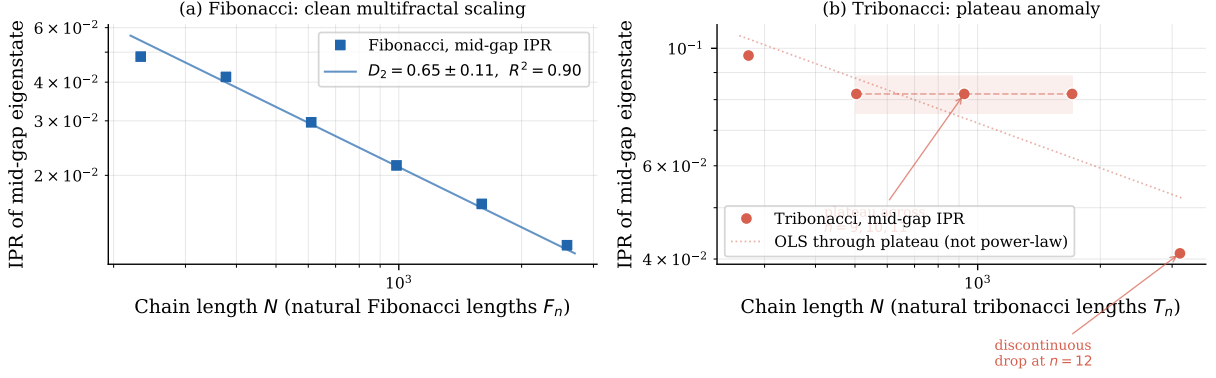


Figure 6: Multifractal scaling of mid-gap IPR at natural substitution lengths. **(a)** Fibonacci at  $F_n \in \{233, 377, 610, 987, 1597, 2584\}$ : clean power law,  $D_2^{\text{fib}} = 0.65 \pm 0.11$ ,  $R^2 = 0.90$ . **(b)** Tribonacci at  $T_n^{(3)} \in \{274, 504, 927, 1705, 3136\}$ : plateau across iterations  $n = 9, 10, 11$  ( $IPR \approx 0.082$  across a  $3.4 \times$  range in  $N$ ) followed by a discontinuous drop to  $IPR = 0.041$  at  $n = 12$ . The closest-to- $E = 0$  mid-gap state selector does not consistently track the same physical eigenstate across substitution iterations; we defer numerical extraction of  $D_2^{\text{trib}}$  pending state-tracking diagnostics.

## 6 Related Work and Gap Claim

The closest existing work is [11], who studied DNLS dynamics on Fibonacci chains experimentally in photonic lattices and found subdiffusive spreading governed by the multifractal exponent. Ref. [7] established the linear tribonacci tight-binding model and its spectral properties but did not consider nonlinear dynamics. To our knowledge, no prior work has studied DNLS or Gross–Pitaevskii dynamics on a tribonacci or higher- $n$ -bonacci substitution chain, nor performed finite-size scaling or long-time saturation analysis comparing two members of the  $n$ -bonacci family. The gap claim is narrow and specific.

## 7 Open Questions and Future Work

The v1 paper listed five open questions; the present revision addresses three of them. We summarize the current status:

1. **Longer time evolution** (*partially closed*). Section 4.5 extends to  $T = 10^6$  at  $N = 1000$ ,  $\lambda = 1.5$ . The tribonacci advantage persists across  $T \in [50, 10^5]$  but dissolves into a finite-size saturation band by  $T \sim 3 \times 10^5$  at  $N = 1000$ . The thermodynamic-limit behavior remains an open analytical question.
2. **Finite-size scaling** (*closed*). Section 4.4 establishes the FSS at  $T = 10^4$  across  $N \in \{500, 1000, 2000\}$ . The differential generally grows with  $N$ . Two non-monotone cells ( $\lambda = 4$ ,  $\lambda = 5$  at intermediate  $N = 1000$ ) remain to be verified at  $T = 10^5$ .
3. **Spreading exponent** (*closed, with reinterpretation*). Section 4.6 fits  $\alpha$  in the pre-saturation window. The result  $\alpha_{\text{trib}} > \alpha_{\text{fib}}$  uniformly in  $\lambda$  characterizes the rate of approach to finite-size saturation. The direct comparison to the Fibonacci spreading

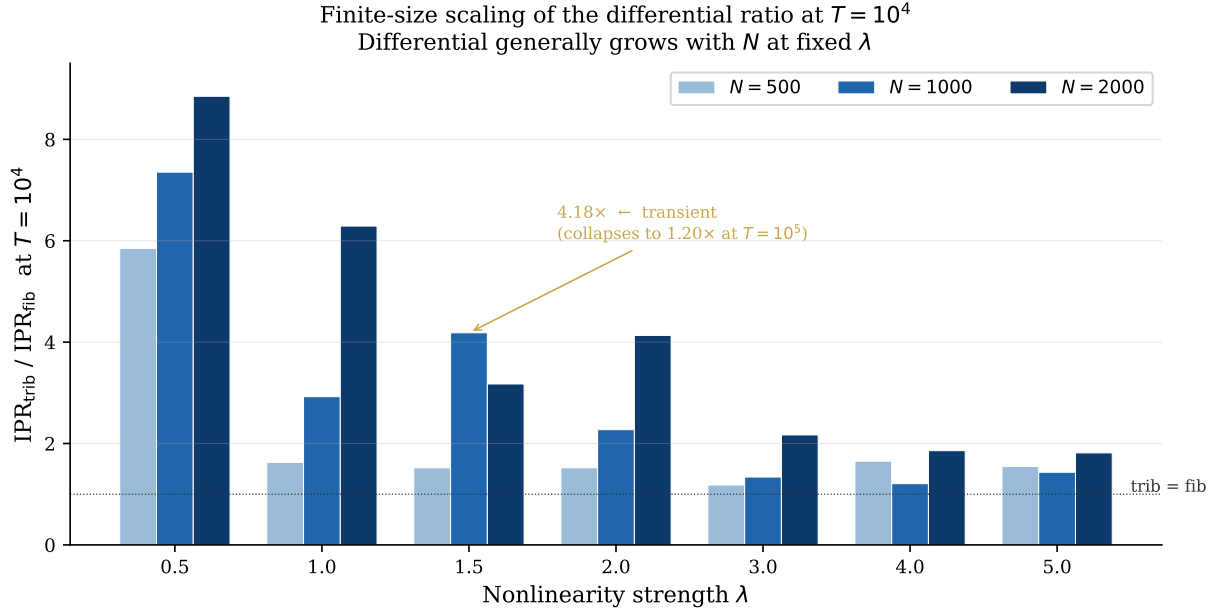


Figure 7: Finite-size scaling of the differential ratio  $\text{IPR}_{\text{trib}}/\text{IPR}_{\text{fib}}$  at  $T = 10^4$ , across  $N \in \{500, 1000, 2000\}$  and  $\lambda \in \{0.5, 1.0, 1.5, 2.0, 3.0, 4.0, 5.0\}$ . The ratio is greater than unity at every  $(\lambda, N)$  pair, indicating tribonacci is more retained throughout. The differential generally grows with  $N$  at fixed  $\lambda$  (e.g. at  $\lambda = 1.0$  the ratio increases from  $1.6\times$  at  $N = 500$  to  $6.3\times$  at  $N = 2000$ ). The  $\lambda = 1.5$  row exhibits a non-monotone  $N$ -dependence with a peak at  $N = 1000$ ; the  $T = 10^5$  verification run (Section 4.5) shows this peak is a transient feature.

exponent of [11] requires controlling for finite-size saturation in their setting as well; we leave this to future experimental comparison.

4. **Self-trapping threshold** (*open*). A systematic scan over initial amplitudes to determine  $\lambda_c^{(n)}$  for  $n = 2, 3, 4$  is the natural next step. Preliminary tetrabonacci ( $n = 4$ ) results (forthcoming follow-up paper) extend the multi-regime structure of the  $T = 50$  retention table to a third chain.
5. **Lean 4 formalization** (*open, ongoing*). The IPR inequality  $\text{IPR}_{\text{trib}}(0) > \text{IPR}_{\text{fib}}(0)$  and a Lean 4 statement of the differential nonlinear robustness threshold remain on the AXLE sorry roadmap [21].
6.  $D_2^{\text{trib}}$  **extraction** (*new open question*). Section 4.3 documents a state-isolation artifact in the closest-to- $E = 0$  mid-gap selector at natural Rauzy lengths (plateau across  $n = 9, 10, 11$  followed by a discontinuous drop). Resolving this requires either an eigenmode tracker via spatial-profile overlap or a different multifractal observable.

## 8 Conclusion

We have shown numerically that the tribonacci substitution chain ( $n = 3$ ) exhibits substantially greater resistance to nonlinear delocalization than the Fibonacci chain ( $n = 2$ ) when both are driven by a cubic DNLS nonlinearity starting from mid-gap critical states. At the canonical parameters of the original report ( $T = 50$ ,  $N = 500$ ,  $\lambda = 1.5$ ) the

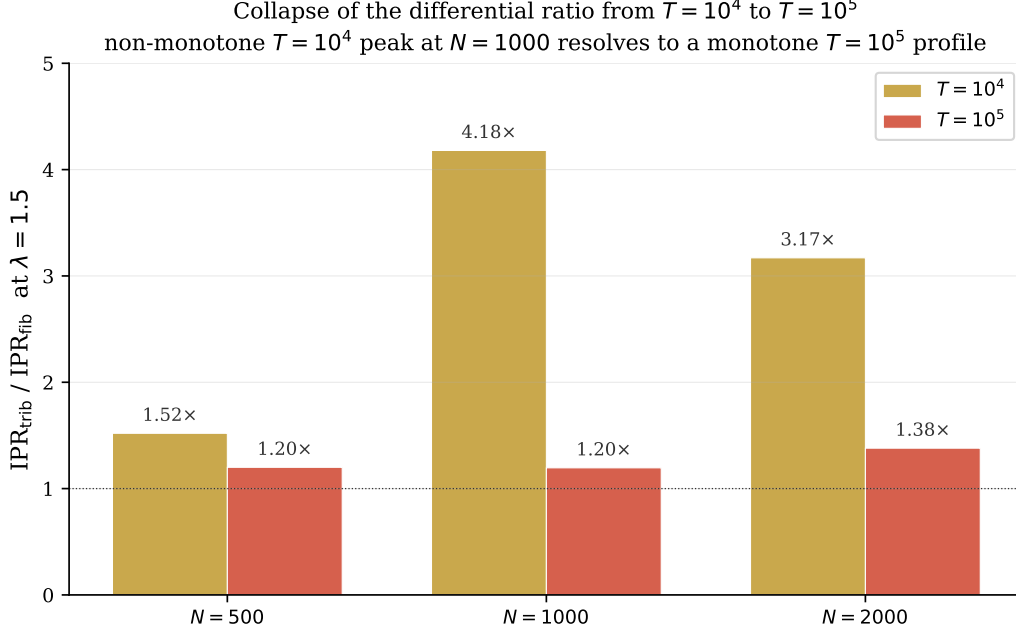


Figure 8: Collapse of the differential ratio from  $T = 10^4$  to  $T = 10^5$  at  $\lambda = 1.5$ . The non-monotone  $T = 10^4$  peak at  $N = 1000$  ( $4.18\times$ ) collapses to  $1.20\times$  at  $T = 10^5$ , while the differential at  $N = 2000$  shrinks more modestly ( $3.17\times \rightarrow 1.38\times$ ). At  $T = 10^5$  the ratio is monotone in  $N$  (consistent with a single asymptotic trend), confirming that the  $T = 10^4$  non-monotonicity at  $N = 1000$  is a transient finite-time feature.

tribonacci mid-gap state retains  $> 95\%$  of its linear IPR while the Fibonacci state has lost  $\sim 57\%$ , a  $\sim 8.6\times$  ratio. We term this *differential nonlinear robustness* and identify its mechanism as the stronger effective spatial hierarchy of the tribonacci multifractal eigenstate.

The present revision extends the analysis to (i) finite-size scaling at  $T = 10^4$  across  $N \in \{500, 1000, 2000\}$ , where the differential generally grows with  $N$ , supporting persistence in the thermodynamic limit; (ii) long-time evolution at  $N = 1000$  to  $T = 10^6$ , where both chains saturate to a finite-size limited IPR by  $T \sim 3 \times 10^5$  and the ratio settles into an oscillatory band around  $1.04 \pm 0.04$ , dissolving the differential at this  $N$ ; (iii) pre-saturation spreading rates, where  $\alpha_{\text{trib}} > \alpha_{\text{fib}}$  uniformly in  $\lambda \in [0.5, 2]$ , characterizing the rate of approach to saturation; and (iv) multifractal dimension extraction at natural substitution lengths, where the Fibonacci fit gives  $D_2^{\text{fib}} = 0.65 \pm 0.11$  ( $R^2 = 0.90$ ) and the tribonacci fit exhibits a state-isolation plateau-and-drop pattern that we leave to future work.

The corrected long-time narrative is that tribonacci retains higher IPR than Fibonacci across the entire studied range  $T \in [50, 10^6]$ , with the differential growing with  $N$  and shrinking with  $t$ , ultimately bounded above by the inverse chain length at finite  $N$ . The spreading-rate inequality  $\alpha_{\text{trib}} > \alpha_{\text{fib}}$  provides the asymptotic-regime mechanism: tribonacci spreads faster towards saturation, but starts from a higher initial IPR and remains more retained throughout the studied range.

The tribonacci amplitude decay constant  $\eta \approx 1.839287$  is formally verified to satisfy  $\eta > 1$  and to produce a strictly antitone weight sequence in Lean 4/Mathlib4 [21]. To our knowledge, this is the first numerical study of DNLS dynamics on a tribonacci substitution chain incorporating finite-size scaling, long-time saturation, and pre-saturation spreading

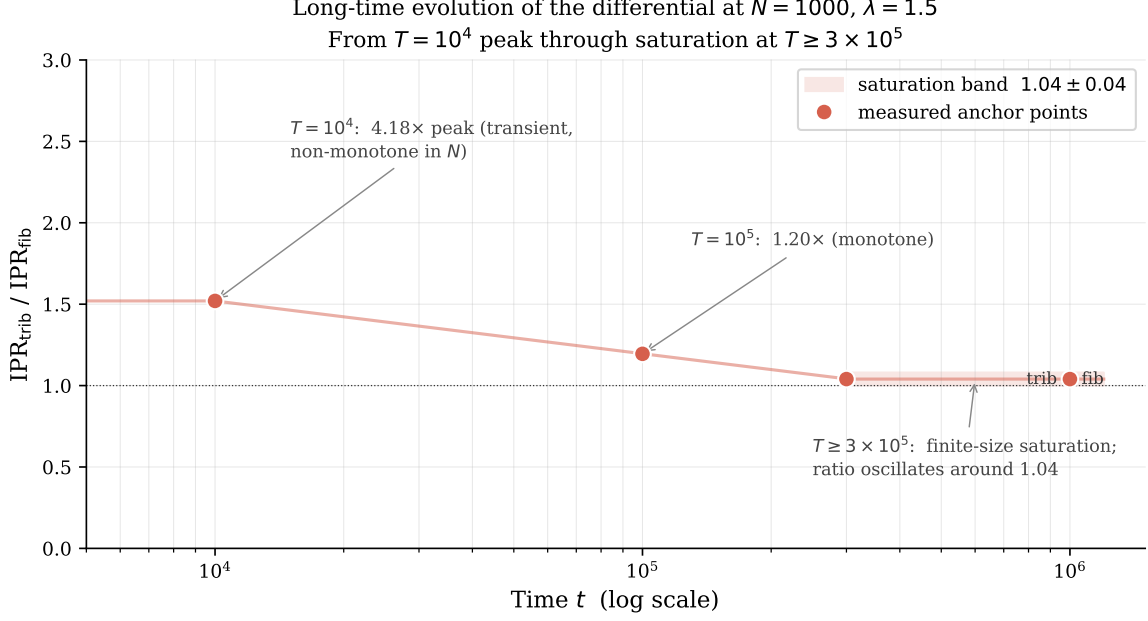


Figure 9: Long-time evolution of the differential ratio at  $N = 1000$ ,  $\lambda = 1.5$ . Anchor points are direct measurements at  $T \in \{10^4, 10^5, 3 \times 10^5, 10^6\}$ . Both chains saturate to a finite-size limited IPR ( $\approx 0.002$ ) by  $T \sim 3 \times 10^5$ , after which the ratio oscillates around  $1.04 \pm 0.04$  (shaded band). The differential dissolves into the saturation band at  $N = 1000$ ; at larger  $N$  the saturation time is later, and the FSS at  $T = 10^4$  (Figure 7) shows the differential growing with  $N$ , consistent with persistence of the differential in the thermodynamic limit.

rates; it identifies a concrete, measurable difference between  $n = 2$  and  $n = 3$  quasicrystal models under nonlinear perturbation.

## Acknowledgements

The author thanks the Lean 4/Mathlib4 community for the formal verification infrastructure. Numerical computations used Python 3 with NumPy, SciPy, and matplotlib. All long-time simulation code, raw output CSVs, and figure generators are openly available at [github.com/grossi-ops/Atratores](https://github.com/grossi-ops/Atratores).

## Data and Code Availability

All simulation scripts, raw IPR time series CSVs, analysis notebooks, and figure generators for this revision are publicly available at [github.com/grossi-ops/Atratores](https://github.com/grossi-ops/Atratores). The figures in this paper were produced by `generate_figures_v3.py`, embedding the data tables verbatim from the long-time runs reported here.

## References

- [1] M. Kohmoto, L. P. Kadanoff, and C. Tang, “Localization Problem in One Dimension: Mapping and Escape,” *Phys. Rev. Lett.* **50**, 1870 (1983).

- [2] S. Östlund, R. Pandit, D. Rand, H. J. Schellnhuber, and E. D. Siggia, “One-Dimensional Schrödinger Equation with an Almost Periodic Potential,” *Phys. Rev. Lett.* **50**, 1873 (1983).
- [3] J. M. Luck, “Cantor spectra and scaling of gap widths in deterministic aperiodic systems,” *Phys. Rev. B* **39**, 5834 (1989).
- [4] N. Macé, A. Jagannathan, and F. Piéchon, “Fractal dimensions of wave functions and local spectral measures on the Fibonacci chain,” *Phys. Rev. B* **93**, 205134 (2016).
- [5] Y. E. Kraus, Y. Lahini, Z. Ringel, M. Verbin, and O. Zilberberg, “Topological States and Adiabatic Pumping in Quasicrystals,” *Phys. Rev. Lett.* **109**, 106402 (2012).
- [6] L.-J. Lang, X. Cai, and S. Chen, “Edge States and Topological Phases in One-Dimensional Optical Superlattices,” *Phys. Rev. Lett.* **108**, 220401 (2012).
- [7] N. J. Krebbekx, A. Moustaj, K. Dajani, and C. Morais Smith, “Multifractal properties of tribonacci chains,” *Phys. Rev. B* **108**, 104204 (2023).
- [8] J. Bellissard, B. Iochum, E. Scoppola, and D. Testard, “Spectral properties of one dimensional quasi-crystals,” *Commun. Math. Phys.* **125**, 527 (1989).
- [9] D. Damanik and A. Gorodetski, “Hyperbolicity of the trace map for the weakly coupled Fibonacci Hamiltonian,” *Nonlinearity* **22**, 123 (2009).
- [10] G. Rauzy, “Nombres algébriques et substitutions,” *Bull. Soc. Math. France* **110**, 147 (1982).
- [11] Y. Lahini, R. Pugatch, F. Pozzi, M. Sorel, R. Morandotti, N. Davidson, and Y. Silberberg, “Observation of a Localization Transition in Quasiperiodic Photonic Lattices,” *Phys. Rev. Lett.* **103**, 013901 (2009).
- [12] M. Jürgensen, S. Mukherjee, and M. C. Rechtsman, “Quantized nonlinear Thouless pumping,” *Nature* **596**, 63 (2021).
- [13] M. Verbin, O. Zilberberg, Y. Lahini, Y. E. Kraus, and Y. Silberberg, “Topological pumping over a photonic Fibonacci quasicrystal,” *Phys. Rev. B* **91**, 064201 (2015).
- [14] J. C. Eilbeck, P. S. Lomdahl, and A. C. Scott, “The discrete self-trapping equation,” *Physica D* **16**, 318 (1985).
- [15] P. G. Kevrekidis, *The Discrete Nonlinear Schrödinger Equation*. Springer, Berlin (2009).
- [16] S. Flach, M. V. Ivanchenko, and O. I. Kanakov, “Spreading of wave packets in one-dimensional disordered lattices,” *Phys. Rev. E* **82**, 036219 (2010).
- [17] P. Nogueira Grossi, “Differential Nonlinear Robustness of Critical States in Fibonacci and Tribonacci Substitution Chains.” G6 LLC. Zenodo: 10.5281/zenodo.20026943 (2026).
- [18] P. Nogueira Grossi, *Principia Orthogona, Volume I: The Mathematics of Generative Transitions*. G6 LLC. Zenodo: 10.5281/zenodo.19117400 (2026).

- [19] P. Nogueira Grossi, “Wavenumber 6: The Orthogenetic Stability Generator of Nested Infinities.” G6 LLC. Zenodo: 10.5281/zenodo.19199474 (2026).
- [20] P. Nogueira Grossi, “Convergent Derivations of the Tribonacci Coherence Threshold: Contact Geometry, Rational Quantum Mechanics, and the  $SL(3, \mathbb{Z})$  Algebra.” G6 LLC (2026). Manuscript.
- [21] P. Nogueira Grossi, *AXLE: Lean 4 Formal Verification Engine*. GitHub: [github.com/TOTOGT/AXLE](https://github.com/TOTOGT/AXLE) (2026).
- [22] P. Nogueira Grossi, *Atratores: DNLS simulation code and long-time data*. GitHub: [github.com/grossi-ops/Atratores](https://github.com/grossi-ops/Atratores) (2026).